Materials Today Bio 12 (2021) 100168

Contents lists available at ScienceDirect

Materials Today Bio

journal homepage: www.journals.elsevier.com/materials-today-bio

Smartphone-integrated colorimetric sensor array-based reader system and fluorometric detection of dopamine in male and female geriatric plasma by bluish-green fluorescent carbon quantum dots

Gayathri Chellasamy [a], Seshadri Reddy Ankireddy [b], Kook-Nyung Lee [c], Saravanan Govindaraju [a,**], Kyusik Yun [a,*]

[a] Department of Bionanotechnology, Gachon University, Gyeonggi-do, 13120, Republic of Korea
[b] Department of Chemical Sciences, Dr. Buddolla's Institute of Life Sciences, Tirupathi, 517503, India
[c] IVD Device Research Institute, Wizbiosolutions, Inc., Gyeonggi-do, 13209, Republic of Korea

ARTICLE INFO

Keywords:
Bluish green carbon quantum dots
Naked eye detection
Smartphone platform
Fluorometric sensing
Dopamine
Geriatric plasma

ABSTRACT

A simple, cost-effective system was developed for dopamine (DA) detection using green synthesized 1–6 nm honey-based carbon quantum dots (H-CQDs) exhibiting bluish green fluorescence. The H-CQDs exhibited emission at 445 nm, with a quantum yield of ~44%. The H-CQDs were used as a probe for electron transfer based DA detection and changes in H-CQD color in the presence of DA. The H-CQDs were formed with polar functional groups and were highly soluble in aqueous media. In the fluorometric mode, the proposed system demonstrated high specificity toward DA and effective limit of detection (LOD) values of 6, 8.5, and 8 nM in deionized (DI) water, male geriatric plasma, and female geriatric plasma, respectively, in the linear range 100 nM–1000 μM. In the colorimetric mode, the color changed within 5 min, and the LOD was 163 μM. A colorimetric sensor array system was used to precisely detect DA with a smartphone-integrated platform using an in house built imaging application and an analyzer app. Additionally, no additives were required, and the H-CQDs were not functionalized. More importantly, the H-CQDs were morphologically and analytically characterized before and after DA detection. Because the sensor array-based system allows high specificity DA detection in both DI water and geriatric plasma, it will play an important role in biomedical applications.

1. Introduction

Dopamine (DA), a signaling molecule, plays an important role as a neurotransmitter in normally functioning nervous systems. DA deficiency and malfunctions are linked to several disorders such as Parkinson's disease and schizophrenia in elderly people [1,2]. Moreover, DA is an extra synaptic messenger, and most approaches for treating addictions focus on DA because all drugs affect the dopaminergic pathway [3]. Traces of DA have been found in blood, and the DA concentration may increase or decrease depending on disease origins and characteristics [4]. Under physiological conditions in nervous systems and bodily fluids, the usual DA concentration range is 10–1000 nM [5,6]. Therefore, owing to various important aspects of pathophysiology, DA must be precisely and selectively detected at the lowest characteristic concentration in biological systems to contribute to the diagnosis of neurological diseases. Several methods of detecting DA concentration have been developed, including electrochemical detection, liquid chromatography (LC) [7], capillary electrophoresis (CE) [8], microdialysis coupled with high performance liquid chromatography (HPLC) [9], fast scan cyclic voltammetry (CV) [10], Mass Spectrometry (MS) [11], Raman Spectroscopy [12]. Although critical advances have been made in DA detection using these techniques, a few drawbacks and limitations remain. For instance, owing to the electroactive characteristics of DA, electrochemical sensing is the method most used to detect DA [13,14]. Nevertheless, because other molecules such as uric acid (UA) and ascorbic acid (AA) exhibit potentials that approximate the DA potential, selective detection is limited using electrochemical methods. The conventional chromatographic techniques require sophisticated instrumentation setup and experts to handle the equipment, they have major disadvantages such as poor temporal resolutions, small sample volume capacities, and large

* Corresponding author.
** Corresponding author.
E-mail addresses: biovijaysaran@gmail.com (S. Govindaraju), ykyusik@gachon.ac.kr (K. Yun).

https://doi.org/10.1016/j.mtbio.2021.100168
Received 24 August 2021; Received in revised form 22 November 2021; Accepted 23 November 2021
Available online 25 November 2021

time consumption during separation and analysis. The advantages of the fluorometric and colorimetric sensor array-based system over other available methods are summarized in Table S1. Optical detection techniques involving the use of fluorometric and colorimetric sensors coupled with nanoparticles have been proposed over the past decade to overcome these obstacles [15–18].

Fluorometric and colorimetric sensors coupled with nanomaterials have been extensively applied to rapidly and selectively detect DA. In the fluorometric detection of DA, either the quenching or enhancement of the employed nanoparticles is measured. The fluorescence based technique has attracted more attention because of its exceptional features such as minimal cost, simple handling, and comparatively high selectivity and specificity. Extensive research has been dedicated to developing fluorescent probes to effectively detect DA [19]. In addition, various probes such as graphene quantum dots, functionalized carbon quantum dots, metal organic framework materials, and nanoclusters have been developed for detecting DA [20–23]. Changes in light absorption, which are observed directly by the naked eye or quantified spectroscopically, are assessed in colorimetric detection [24]. Considering the characteristics of these advanced techniques, combining fluorometric and colorimetric detections would greatly enhance DA detection. In recent years, smartphone-based biosensing platforms have rapidly emerged because of their handiness, ubiquity, and accessibility. With advancements in highly featured smartphone cameras and image quality, smartphones have been broadly coordinated with fluorescence, colorimetric, and electrochemical biosensors. The added advantage of mobile phones is the convenient use of in-house-built Android/I OS based applications, which eliminates desktop data/image processing. In particular, smartphones have effectively been incorporated with colorimetric detection owing to their expected ongoing applications to biomedical and environmental studies [25].

Some of the most prominent nanoparticles used in optical sensors are gold nanoparticles (AuNPs), silver nanoparticles (AgNPs), copper nanoparticles (CuNPs), and fluorescent carbon quantum dots (CQDs) [26–29]. Most DA detection methods utilize an additive such as an enzyme, an aptamer, or a deoxyribonucleic acid (DNA) template, and in some cases, nanoparticles are chemically modified and functionalized. However, these characteristics limit the cost effectiveness, robustness, and subsequent application of the resulting sensors. In contrast, CQD based DA detection has attracted considerable attention because of its source availability, better fluorescent characteristics, water solubility, selectivity, and sensitivity [30,31]. Recently, dual-mode detection using gold nanoclusters (AuNCs) coupled with aptamers and enzymes has been reported [32].

DA usually is readily detected in geriatric plasma because elderly persons have considerably high levels of plasma DA and exhibit high interindividual distinctions [33]. Moreover, numerous research reports and methods are available for analyzing serum and plasma samples. Perhaps this is the first report on DA detection in male and female geriatric plasma by smartphone-integrated fluorometric and colorimetric methods using eco-friendly and environmentally benign honey-derived CQDs (H-CQDs). Moreover, to the best of our knowledge, smartphone-integrated, additive free, nonfunctionalized CQD based fluorometric and colorimetric DA detection has not yet been reported.

Therefore, in this study, we report dual-mode DA detection by integrating a sensor array-based reader system with H-CQDs to detect DA in male and female geriatric plasma. Our study aimed to synthesize water soluble CQDs by a quick (~20 min), cost-effective, and environment friendly approach. We utilized honey as the carbon source and sodium hydroxide (NaOH) as the reducing agent to synthesize H-CQDs by microwave assistance. In the fluorometric mode, DA was detected by the electron transfer between the H-CQDs and the DA. In the colorimetric mode, the H-CQD bound DA formed DA-*O*-hydroquinone (DQ), thereby changing the color of the H-CQD solution. In the sensor array-based reader system, the color change was readily analyzed using a smartphone and an Android-OS-based image analysis application. We chose male and female geriatric plasma as the biological media because DA-related disorders such as Parkinson's disease, Alzheimer's disease, and schizophrenia are more common among older people. For further confirmation, high performance liquid chromatography (HPLC) was performed to detect DA in biological samples for comparative analysis. Compared with other DA detection techniques, our system effectively detected DA in biological samples, dual-mode DA detection with a sensor array-based reader system provides additional advantages such as consistency, cost effectiveness, and rapid analysis. Moreover, it provides qualitative and quantitative results for DA detection in deionized (DI) water and biological samples, which could be practically applied to clinically diagnose geriatric patients.

2. Experimental methods

2.1. Chemicals

Food grade honey (Natural honey 90%, Miscellaneous Honey 10% Carbon isotope ratio-12%) was purchased from a local market in South Korea. Sodium hydroxide (>97.0%), dopamine hydrochloride (98%), glucose (99.5%), sodium chloride (99.0%), potassium chloride (99.0%), magnesium chloride (>98.0%), and calcium chloride (>97%), Iron (III) chloride hexahydrate (97%), Iron (II) chloride tetrahydrate (98%), Aluminum chloride hexahydrate (99%), Zinc nitrate hexahydrate (98%), L-Aspartic acid (>98%), L-Cysteine (97%), Uric Acid (UA) (>99%), L-Glutathione reduced (>98%), were all purchased from Sigma Aldrich (USA). Plasma samples from male and female geriatric patients were obtained from Lee BioSolutions, Inc. (USA). DI water prepared using a Milli-Q® purification system (Millipore, USA) was used for all the experiments.

2.2. Instrumentation

An ATTO ultraviolet (UV) transilluminator was used to obtain luminescent images of the H-CQDs irradiated at 365 nm. A Varian Cary 100 UV–visible (UV–vis) spectrophotometer was used to record the UV–vis absorption spectra. Photoluminescence (PL) spectra were recorded using a SCINCO FS-2 fluorescence spectrometer equipped with FluoroMaster Plus software, a 150-W continuous-wave xenon arc lamp, and a high-performance R-928 photomultiplier tube (PMT) detector. High-resolution transmission electron microscopy (HR-TEM) and energy dispersive X-ray spectroscopy (EDS) were performed using a Tecnai™ G2 F30-Series microscope. The H-CQD height was obtained using bioatomic force microscopy (Bio-AFM, JPK NanoWizard® II bioatomic force microscope, Berlin, Germany). An A1-Kα radiation source (15 kV, 100 W, 400 μM) equipped with sigma-probe X-ray photoelectron spectroscopy (XPS) was employed to chemically analyze the elemental contents of the H-CQDs in the presence and absence of DA. Fourier transform infrared spectroscopy (FTIR) was performed using a JASCO FT/IR 4600 spectrometer equipped with spectral analysis software. Surface charge was analyzed using a NanoBrook ZetaPALS (phase analysis light scattering) analyzer (Brookhaven Instruments). Raman spectral analysis was performed using a micro Raman system (Ramboss 500i) with an He–Ne laser beam at 633 nm. The quantum yield (QY) of the H-CQDs was measured using a Fluoro-Q2100 Quantum Yield system operating at an excitation wavelength of 450 nm. Lifetime decay curves were recorded using a Photon Technology International (PTI) EL series of nanosecond pulsed light emitting diodes (LEDs) designed for EasyLife™ II (Horiba). A microwave oven was used to heat the solution, dissolve the honey, and synthesize the H-CQDs. Dialysis tubing (molecular weight cutoff: 1 kDa) was purchased from Spectrum Chemical Mfg.

2.3. Synthesis of H-CQDs

H-CQDs were synthesized using microwave assistance. In brief, honey (5.0 g) and distilled water (25 mL) were mixed using a magnetic stirrer to

uniformly dissolve the honey in the water. The solution was then heated to ~100 °C in a microwave oven for 10 min, and 5 mL of 0.5 M NaOH solution was added. The mixture was stirred and heated in a microwave oven (~100 °C) for up to 10 min to obtain the H-CQDs, as confirmed by analyzing the fluorescence of the obtained solution in a UV trans-illuminator operating at 365 nm. Finally, the H-CQDs were filtered using filter paper, dialyzed using a membrane (molecular weight cutoff: 1 kDa) against DI water for 12 h to purify them, and stored at 4 °C. The reaction conditions pertaining to the pH, solvent, different honey were optimized before synthesizing the H-CQDs. Followed by the quantum yield of as-synthesized H-CQDs were assessed by five point standard quinine sulphate (QS) approach. Simultaneously biocompatibility of the as-synthesized H-CQDs was analyzed.

2.4. Fluorometric detection of DA using H-CQDs

DA biosensing was performed by directly combining the H-CQDs and the DA after the H-CQDs had been sonicated for a few seconds in a bath to bring them to the ambient temperature. Throughout the experiment, the H-CQDs concentration was maintained at 1.8 mg/mL. The fluorometric spectra were obtained as follows: 3 mL of DI water and 100 μL each of H-CQDs and DA were added to a cuvette, mixed well by pipetting, and incubated for approximately 10 min. The incubated mixture was then subjected to fluorescence measurements. DA was detected at concentrations ranging from 100 nM to 100 μM, and each measurement was performed three times to standardize the results and establish a repeatability protocol. Complete DA detection by fluorometric assay required approximately 15 min, including an incubation period of approximately 10 min and a response readout time of approximately 5 min.

2.5. Colorimetric sensor array-based reader system for DA detection

For colorimetric DA detection, solutions were prepared using various DA concentrations ranging from 1000 μM to 100 mM. Then, 200 μL each of H-CQDs and the prepared DA (1000 μM–100 mM) solutions were added to different wells in a well plate, and the color change was observed. The DA detection response time was approximately 5 min to observe the color change. The same mixture was used to quantify the DA concentration by UV–vis spectroscopy. To precisely detect DA colorimetrically, we used a colorimetric sensor array-based reader system housed in a unit to maintain a constant position for the sensor array into which the samples were loaded and imaged using an Android OS-based application. The acquired images were analyzed using an app to obtain the color difference of the sensor array.

2.6. Detection of DA in geriatric plasma

DA was detected in biological samples of male and female geriatric plasma according to a method previously described elsewhere in the literature [27]. Initially, the plasma was diluted 10 fold using phosphate buffered saline (PBS) solution and was used for further experiments without any purification. Initially, 100 μL of H-CQDs and male geriatric plasma were spiked with DA in concentrations ranging from 100 to 1000 nM in separate cuvettes. The samples were mixed well and were incubated for 10 min, and the PL spectra were measured for the incubated samples. Finally, PL spectra were recorded for the incubated mixtures. For colorimetric DA detection, 200 μL of H-CQDs and 100 μL each of plasma and DA in concentrations ranging from 1000 μM to 100 mM were added to detachable 8-well plates, and the color change was observed. The same mixture was used to quantify the DA concentration by UV–vis spectroscopy. All the measurements were performed separately for the male and female geriatric plasma samples. HPLC experiments were then performed on the samples, and the results were compared with those of our DA detection system.

2.7. Interference experiments

Interferents such as sodium (Na^+), potassium (K^+), calcium (Ca^{2+}), magnesium (Mg^{2+}), chlorine (Cl^-), glucose (Glu), urea, creatinine, ammonia, iron (Fe^{2+} and Fe^{3+}), zinc (Zn^{2+}), aluminum (Al^{3+}), UA, glutathione (GSH), L-aspartate (L-Asp), L-cysteine (L-Cys), Albumin were used for the selectivity study, which was conducted as follows. Interferent solutions (100 μM) were prepared, and 100 μL each of the H-CQDs and the prepared interferent solutions were added to different cuvettes. Next, 3 mL of DI water was added to the cuvettes, the mixtures were incubated for 10 min, and PL spectra were recorded. The same procedure was followed using 100 μL of plasma to analyze the biological samples. For colorimetric DA detection, 1000 μM interferent solutions were prepared, and 200 μL each of H-CQDs and prepared interferents were added to well plates. Then, 200 μL of H-CQDs and 100 μL each of plasma and interferents were added to different well plates, and color changes were observed.

3. Results and discussion

3.1. H-CQDs-synthesis, characterization, mechanism

3.1.1. Synthesis

Herein, we report a rapid, cost-effective method of synthesizing H-CQDs from honey which is rich in both fructose and glucose as a carbon source and NaOH as a reducing agent. The entire synthesis required approximately 20 min, and the honey solution was stirred and heated twice for 10 min once each before and after the NaOH was added to enable the NaOH to readily react with the carbon source and corresponding functional groups and form hydroxyl (–OH), and carbonyl (–C═O) functional groups on the H-CQD surfaces [34]. Because of these functional groups, the as-prepared H-CQDs were remarkably soluble in all types of aqueous media, including DI water, PBS, serum, plasma, and cerebrospinal fluid. The emission of bluish green fluorescence from the final obtained reaction mixture under UV illumination confirmed the formation of the H-CQDs, which were used to detect DA by fluorometric and colorimetric sensors. The optimized H-CQD synthesis route and DA detection working principle are presented in Scheme 1.

3.1.2. Optical properties of H-CQDs

The initial optical properties of the as-prepared H-CQDs were investigated, and the corresponding results are presented as follows; The H-CQDs exhibited bluish green fluorescence emission at 445 nm when excited at 342 nm (Fig. 1a). The inset is a photograph of the as-synthesized H-CQDs, which appeared pale yellow under normal light (Fig. 1a, Inset A), and bluish green luminescence was observed upon UV irradiation at 365 nm, as shown in (Fig. 1a, Inset B). Furthermore, the optical characterization of the H-CQDs by UV–visible absorption spectroscopy showed a distinct peak at 286 nm and a tail extending into the visible range (Fig. 1a) owing to the n–π* transition of the carbonyl (–C═O) functional groups and the π–π * transition of the C═C bonds in the graphitic core of the H-CQDs [35]. PL spectra were generated for the H-CQDs to determine the size dependent PL behavior and the emission wavelength through excitation dependent emission (Fig. 1b). The maximum emission wavelength was observed at 445 nm when the H-CQDs were excited at 342 nm, and the emission peaks red shifted with increasing excitation wavelength. However, the intensity of the emission peaks increased gradually, and the most intense emission was observed at 445 nm when the H-CQDs were excited at 342 nm. Because most CQDs are synthesized from various natural sources using a top down approach, the as-prepared H-CQDs exhibited unique synthesis condition dependent behaviors such as different excitation dependent emission properties. Although several competing mechanisms have been proposed to explain this phenomenon, the exact reason remains unclear. However, density functional theory (DFT) calculations suggest that charge transfer, nanocrystal edge defects, and self-aggregation are the main reasons for this

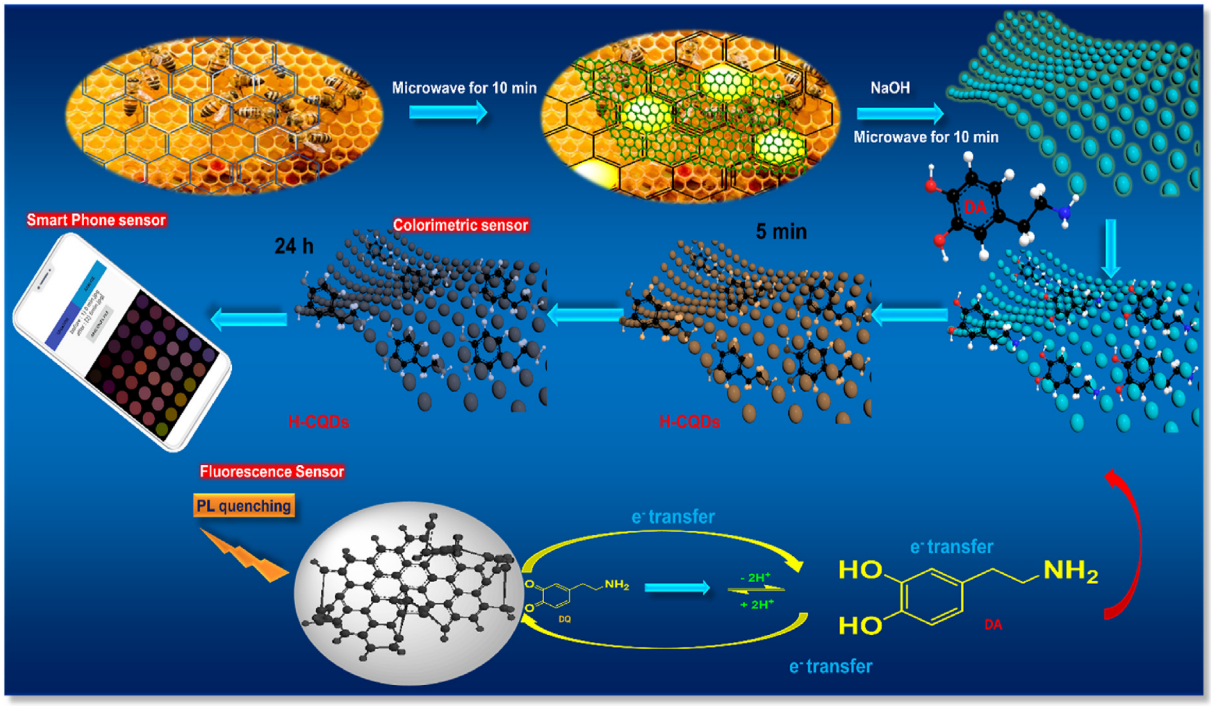

Scheme 1. Schematic illustration of synthesis and working principle for smartphone integrated sensor array reader system for DA detection using H-CQDs.

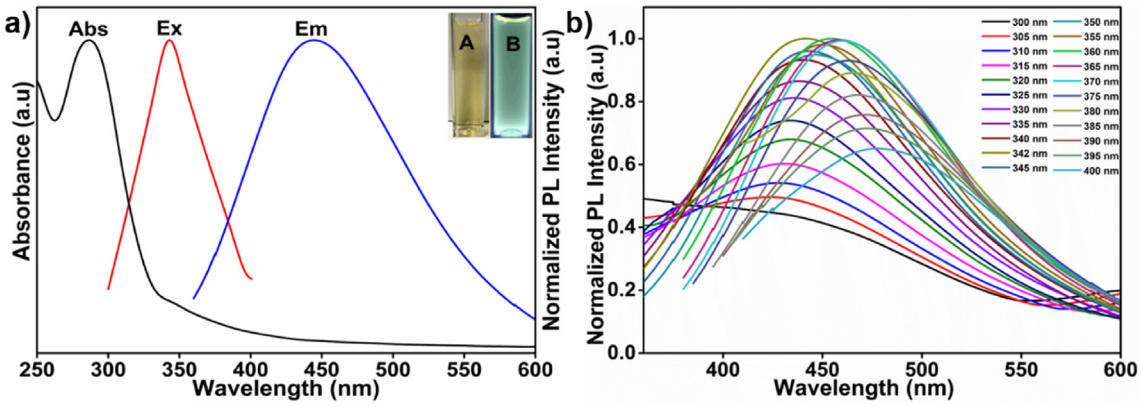

Fig. 1. a) Overlay image of the UV–vis absorption spectrum, Excitation and Emission spectra of H-CQDs, Inset: Photographs of H-CQDs under (A) daylight and (B) UV light (b) Excitation dependent emission spectra of H-CQDs.

phenomenon. In addition, several molecular orbital electronic transitions such as n_N 2*p*–σ*, π–π*, n_O 2*p*–π* (–OH), n_O 2*p*–π* (–COOH), n_O 2*p*–π* (–COO−), and n_N 2*p*–π* transitions from π, n_O 2*p* (–OH), n_O 2*p* (–COOH), n_O 2*p* (–COO−), n_N 2*p*, π*, and σ* excited states are molecularly possible for CQDs. The hydroxyl, carboxyl, and amine functionalities were detected for various electronically excited states. In addition, bonding and antibonding molecular orbitals also play a crucial role in these transitions. Because of this peculiar property, CQDs have also been employed for bioimaging and other medical research applications [36–39].

We used standard QS as a reference to measure the QY of the H-CQDs and used the five point method to theoretically calculate the QY based on the following equation:

$$Q_S = Q_R \times \frac{I_S}{I_R} \times \frac{A_R}{A_S} \times \frac{\eta_S^2}{\eta_R^2} \quad (1)$$

where QS and QR are the QYs of the H-CQDs and QS, respectively; IS and IR are the areas under the PL spectra generated for H-CQDs and QS, respectively; AS and AR are the absorbances of the H-CQDs and QS, respectively; and ηS and ηR are the refractive indices of the H-CQDs and QS, respectively [40]. According to these calculations, the H-CQD QY was 44.7% (Fig. S1).

To optimize the H-CQDs and their PL characteristics, we assessed H-CQDs under various conditions including different pH values, solvents, and time. The results showed that for pH values in the range 2–10, the H-CQDs exhibited the highest PL intensity at pH 7 and were almost stable under basic conditions between pH 7 and 10. (Fig. S2a). The H-CQDs were stable in the different solvents, and the PL was not quenched (Fig. S2b). The H-CQD PL intensity was stable over 15 days for 4.5 months (Fig. S2c), which confirms that the H-CQDs were highly stable for a sustained period. To optimize the reproducibility, we synthesized H-CQDs from different honey purchased from the same market. All the H-

CQDs exhibited unique fluorescence properties and similar PL intensities, as shown in Fig. S3a, b, c, d respectively. Because the H-CQD stability is expressed as a function of λ_{emi}, the PL intensity was reexamined for several batches consisting of a homogeneous mixture of H-CQDs. Clearly, each batch of H-CQDs excited at 445 nm exhibited a unique stability and PL intensity as functions of λ_{emi}. (Fig. S3e and f). Consequently, the fluorescence of the H-CQDs was theoretically visualized as exhibiting an organic moiety consisting of conjugated double bonds lying between electron releasing (–OH and $–NH_2$) and receiving groups (–COOH and –C═O). More importantly, high fluorescence emission can be generated by the well-organized conjugation between the electron releasing and receiving groups. Interestingly, the as-synthesized H-CQDs exhibited –OH and –COOH functionalities as electron releasing and receiving groups, respectively. In contrast, the fluorescence of any nanomaterial can depend on well separated electron hole ($e^- - h^+$) pairs between valence and conductance bands (CBs). Consequently, both theories might be responsible for the high fluorescence emission of the H-CQDs. Interestingly, the calculated high QYs were also in good agreement with those theoretically predicted by the mechanism for the H-CQD fluorescence properties [41]. The biocompatibility of H-CQDs were assessed and it is observed that they were biocompatible up to 100 mg/mL of sample solution which contains 180 μg/mL of drug upon 24 h of sample treatment on HaCaT cells (Fig. S4).

3.1.3. *Morphological and analytical studies of H-CQDs before and after sensing DA*

The H-CQD morphology was characterized using TEM and Bio-AFM. The HR-TEM image shows that the H-CQDs were well distributed particles ranging from 1 to 6 nm. (Fig. 2a–c). The selected area diffraction (SAED) pattern shown in Fig. 2c insert confirms that the H-CQDs are poly nanocrystalline nature [42,43]. HR-TEM images focused on various H-CQDs regions are shown in Fig. S5a-c. The H-CQD lattice spacing was measured as 0.2198 nm which further confirms the crystallinity. EDS analysis showed that the H-CQDs exhibited a high carbon content and traces of N, O, and Na (Fig. S5d). The Bio-AFM height image confirmed that the H-CQDs were well distributed and that few H-CQDs overlapped at a height of 5.94 nm (Fig. 2d) the corresponding particle size distribution showed that individual H-CQDs were smaller than 6 nm (Fig. S5e, f). The corresponding error image (Fig. 2e) and 3D height profile of the H-CQDs (Fig. 2f) were consistent with the HR-TEM images. Prior to DA detection, the H-CQD morphology was characterized, and we then analyzed the morphology of the H-CQDs in the DA containing solutions by HR-TEM and Bio-AFM. HR-TEM analysis showed that the H-CQD particle size had increased tremendously, as shown in Fig. S6a, which depicts H-CQD particles aggregated with DA and particle sizes ranging from 10 to 50 nm. Furthermore, we confirmed this result by Bio-AFM analysis in which the AFM height showed that the aggregated H-CQD height was approximately 10 nm (Fig. S6b).

To analytically characterize the H-CQDs, FTIR spectra were generated to elucidate the surface functional groups. As shown by the red trace in Fig. S7a, the stretching frequencies at 3291, 1641, 1052 cm^{-1} indicates the presence of –OH, C═O, C–O groups, respectively [44]. The black trace in Fig. S7a shows the FTIR spectrum obtained for the DA. The peaks at 3342, 3201, and 3031 cm^{-1} were attributed to the –OH, –CN, and –NH groups, respectively. The peak at 1221 cm^{-1} corresponds to the DA –CH group [45]. The blue trace in Fig. S7a shows the FTIR spectrum obtained for the H-CQDs after DA detection. The corresponding spectrum shows that the –OH group around the 3000 cm^{-1} is reduced and the stretching around 1500–1600 cm^{-1} is increased which attributes the reaction of DA with H-CQDs. The results show H-CQDs functional groups had been

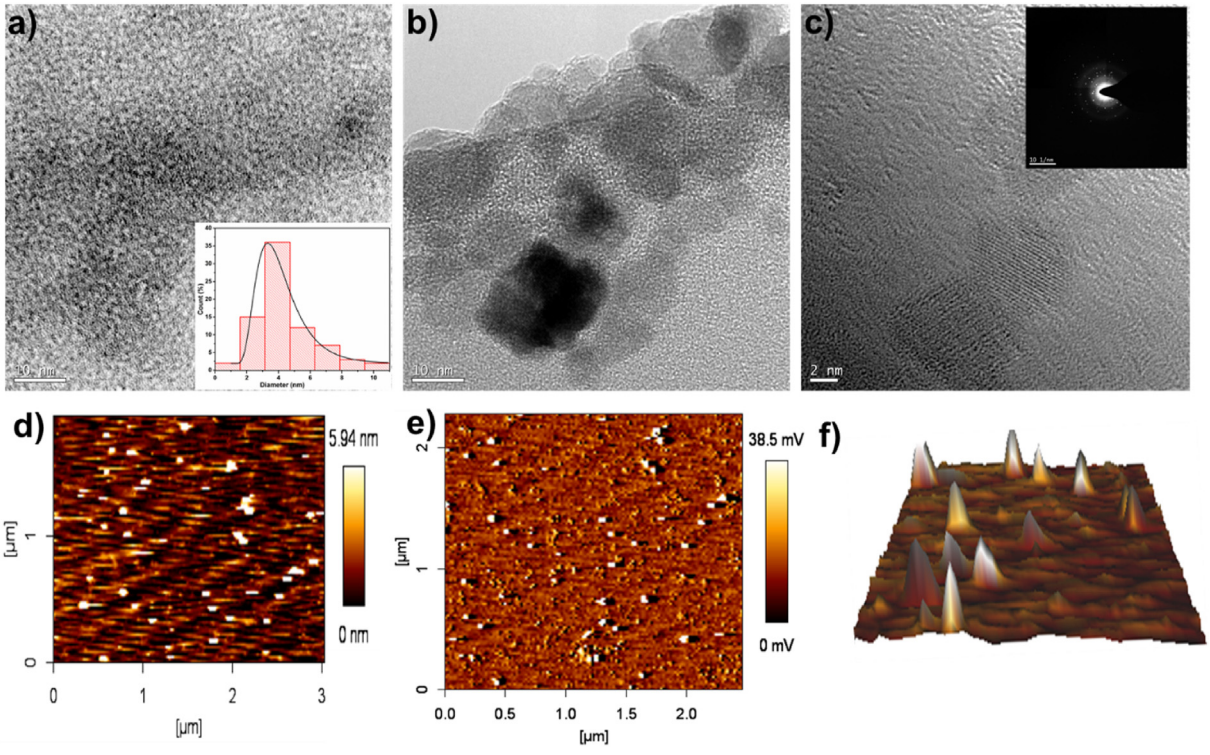

Fig. 2. a-c) HR-TEM images of H-CQDs, a-Inset: Particle size distribution of H-CQDs, c-Insert: SAED pattern (d) Bio-AFM image of H-CQDs, (e) Error image of H-CQDs, (f) 3D image of H-CQDs.

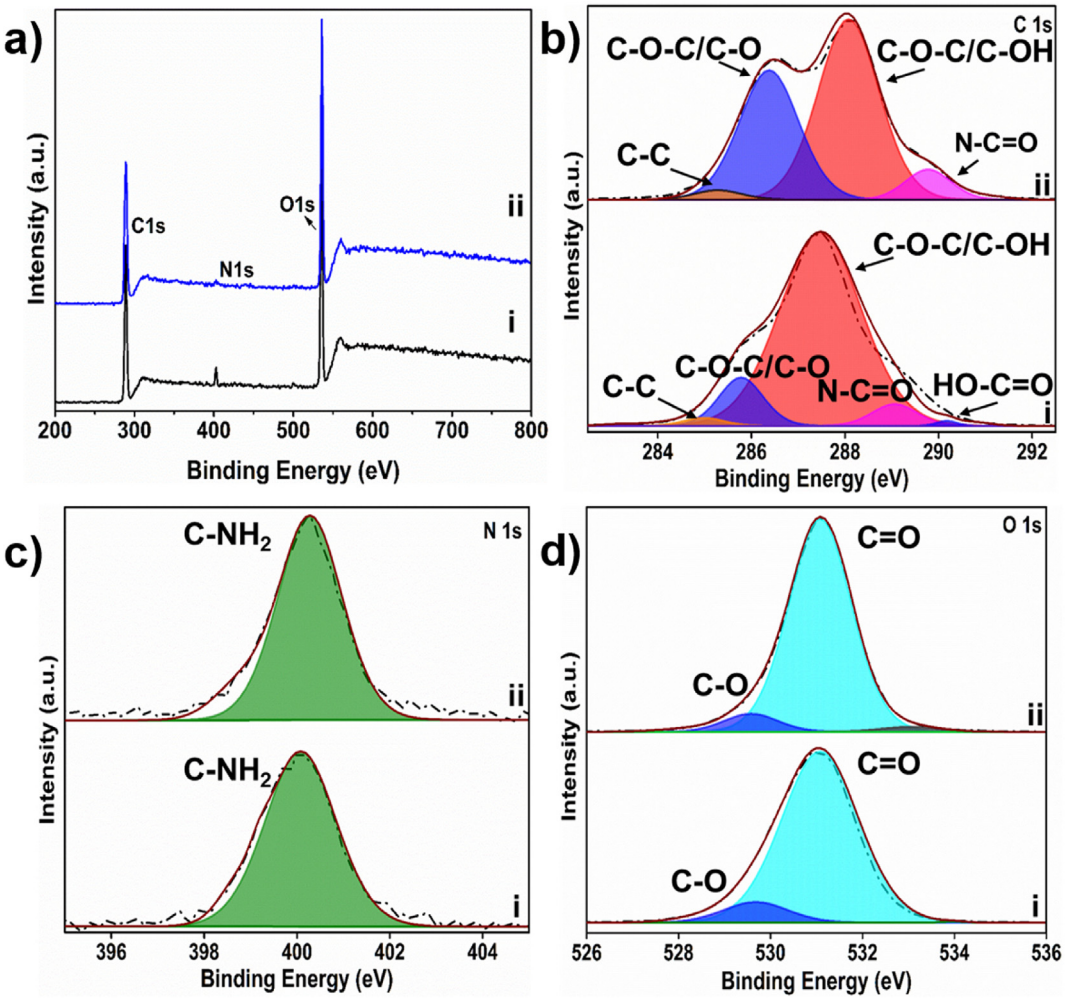

Fig. 3. a) Survey XPS spectra of (i) H-CQDs (ii) H-CQDs + DA, (b–d) Deconvoluted high resolution XPS spectra of C 1s, N 1s, O 1s (i) H-CQDs (ii) H-CQDs + DA.

conformationally changed on addition of DA and it confirmed that DA had been detected by the H-CQDs.

To analyze the complete chemical and elemental composition of the H-CQDs, XPS spectra were generated. The XPS spectra in Fig. 3ai show three major peaks corresponding to C, N, and O at binding energies of 288, 402, and 535 eV, respectively. Furthermore, the high resolution deconvoluted C 1*s* XPS spectra showed peaks corresponding to C–C, C–O–C/C–O, C–O–C/C–OH, N–C═O, and HO–C═O at binding energies of 284.9, 285.7, 287.4, 289, and 290 eV, respectively (Fig. 3bi). The deconvoluted N 1*s* spectra showed a peak at 400 eV, corresponding to the C–NH_2 group (Fig. 3ci). In the O 1*s* spectra, two distinct peaks at 529 and 531 eV were attributed to C–O and C═O, respectively (Fig. 3di) [46]. The XPS spectra (Fig. 3 a–d [ii]) exhibited considerably different peaks after DA detection. The total survey spectrum shown in Fig. 3aii exhibited characteristic peaks at 288, 402, and 535 eV corresponding to C 1*s*, N 1*s*, and O 1*s*, respectively. To further elucidate the H-CQD surface chemistry after DA detection, the individual high resolution C 1*s*, N 1*s*, and O 1*s* spectra were deconvoluted from the total survey spectrum. After DA detection, the deconvoluted C 1*s* spectrum for the H-CQDs (Fig. 3bii) exhibited peaks corresponding to C–C, C–O–C/C–O, C–O–C/C–OH, and N–C═O at binding energies of 285.2, 286.3, 288.08, and 289.78 eV, respectively. Compared to the peak in the spectrum generated for the H-CQDs prior to DA detection, the intensity of the peak at 290 eV corresponding to OH–C═O was weaker, which confirms that DQ had formed by proton transfer thereby quenching the H-CQDs. In addition, peaks like those in the spectrum generated for the H-CQDs prior to DA detection also appeared in the deconvoluted N 1*s* and O 1*s* spectra but were slightly different after DA detection. The FTIR and XPS spectra were consistent, suggesting that the H-CQDs exhibited an enormous concentration of hydroxyl groups and traces of amine groups, thereby facilitating their excellent water solubility.

The Raman spectra of the H-CQDs showed characteristic D band at 1353 cm^{-1} and G band at 1575 cm^{-1} (indicated by the black trace in Fig. S7b), which attributes the similarities of graphitic core and the defect [47]. A downward shift in the D and G bands of H-CQDs after detection of DA as compared to H-CQDs is observed. The intensity ratio I_D/I_G of as prepared H-CQDs is 1.05 whereas the I_D/I_G of H-CQDs after DA detection is 1.04 [48]. In accordance with the SAED pattern and the lattice spacing with I_D/I_G ratio calculated the H-CQDs possess the polycrystallinity [49]. The Raman spectra generated for DA (Fig. S7b Insert) exhibited multiple vibrations in the range of 1000–4000 cm^{-1}, implying the presence of different forms of carbon stretching [50]. To assess the H-CQD surface charge, zeta potentials were measured. The H-CQD surface revealed a charge of −26.98 mV (Fig. S8a), which confirmed that the –OH and –COOH functional groups had contributed to the negative surface charge. The DA surface (Fig. S8b) exhibited a positive charge of approximately

16.59 mV [51]. After DA detection, the H-CQDs exhibited a considerably reduced surface charge of approximately −11.76 mV (Fig. S8c), which confirms that DA had reacted with the H-CQDs thereby leading to DA detection.

3.1.4. Plausible mechanism

According to the foregoing analysis results, we propose a plausible working mechanism for the PL quenching of DA-treated H-CQDs, and corresponding data are shown in Fig. 4. The FTIR and XPS spectra indicated that the H-CQD surfaces exhibited an enormous concentration of hydroxyl functional groups, which almost resembled phenolic moieties. The basic amine functional groups on the DA surfaces catalyzed the initiation of the reaction between the DA and the H-CQDs to avoid PDA formation instead of forming DQ, which eventually quenched the PL intensity of the H-CQDs. The protons on the H-CQD surfaces were highly acidic because of the resonance structures for the ionizable aromatic moieties of the graphitic core. Subsequently, these protons were abstracted by the amine functional groups of the DA treated H-CQDs. Consequently, basic polyphenoxide ions were generated from the H-CQDs and initiated the reaction between the H-CQDs and the DA. In addition, DA exhibits two hydroxyl groups on its benzene ring and excellent redox properties owing to its amazing ionizability ($pK_a \approx 9$) [52]. In contrast, exciton or electron hole pairs were generated from the H-CQDs by the transfer of electrons from the valence band (VB) to the CB to generate sufficient energy ($h\nu$). The DA acidic protons were then abstracted by the negatively charged H-CQD surface and eventually generated stable phenoxide anions on the DA surface because the negative charge of the DA oxygen atom was delocalized through the benzene ring resonance structures and eventually formed the DQ structure, as illustrated in Fig. 4. Finally, electrons flowing from the H-CQD CB to the DA may have formed DQ, which eventually may have quenched the PL intensity of the H-CQDs in the presence of DA [1,53]. When DQ was formed, the ammonium protons could be returned by the H-CQDs. Soon thereafter, intramolecular conjugate addition may have occurred between the amine and α, β unsaturated functional groups of the H-CQDs to form a PDA structure through sequential chain reactions, as presented in Fig. 5. Owing to the formation of PDA molecules, DA interacted with the geriatric plasma, and the reaction mixture considerably darkened after 24 h.

3.2. Sensing of DA using H-CQDs

3.2.1. H-CQDs based fluorometric detection of DA

H-CQDs based fluorometric detection of DA is shown in Fig. 6a. When DA was added in concentrations ranging from 100 nM to 100 μM to the H-CQDs, the fluorescence intensity of the H-CQDs was quenched drastically up to 70%. The relative change in fluorescence intensity is plotted as a linear function of the initial intensity (F_0/F) for H-CQDs excited at 342 nm with DA concentrations in the range 100–1000 nM. The regression coefficient ($R^2 = 0.993$) is presented in the inset of Fig. 6b. The Stern–Volmer equation $F_0/F = Q\,(1 + K_s)$ was used to investigate the relationship between the DA concentration and the quenching efficiency of the H-CQDs, where F_0 and F are the emission intensities generated at 445 nm in the absence and presence of DA, respectively, K_s is the Stern–Volmer constant, and Q is the DA concentration. From the obtained results, we calculated the limit of detection (LOD) as 6 nM according to the formula $LOD = 3S/q$, where S is the standard deviation, and q is the slope of the calibration curve. To further confirm the fluorescence quenching of the H-CQDs in the presence of DA, the prominent lifetime decay was measured to detect electron transfer from the H-CQDs to the DA. The lifetime decay curves were recorded at an excitation wavelength of 342 nm before and after the H-CQDs were treated with DA. The double exponential function was used to fit all the curves as follows:

$$D(t) = \sum_{i=1}^{n} a_i \exp(-t/\tau_i), \tag{2}$$

where D is the fluorescence decay, τ is the lifetime, τ_i is the PL lifetime of various fluorescent species, and a_i is the corresponding preexponential factor. According to the lifetime decay, τ_1 and τ_2 were 14.94 and 1.42 ns, respectively, for the H-CQDs. However, after DA was added to the H-CQDs, τ_1 and τ_2 decreased to 5.8 and 0.081 ns, respectively, which clearly indicated that electrons had transferred from the CB of the H-CQDs to the DQ in 9.14 ns. A representative image of the H-CQD lifetime decay is

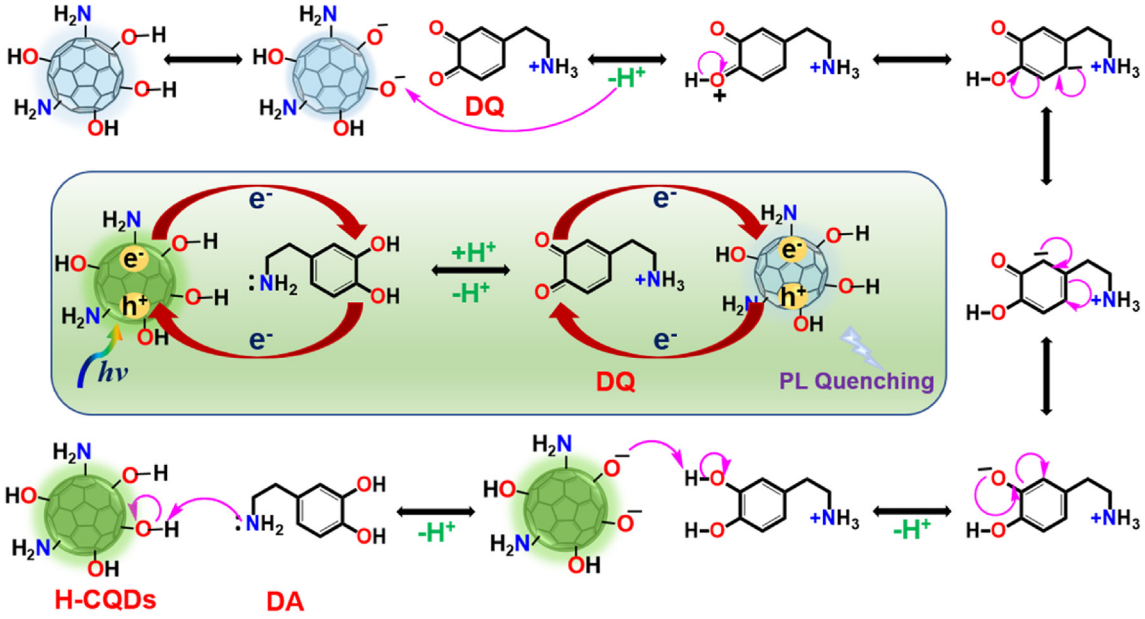

Fig. 4. Schematic representation of plausible working mechanism for PL quenching H-CQDs in the presence of DA.

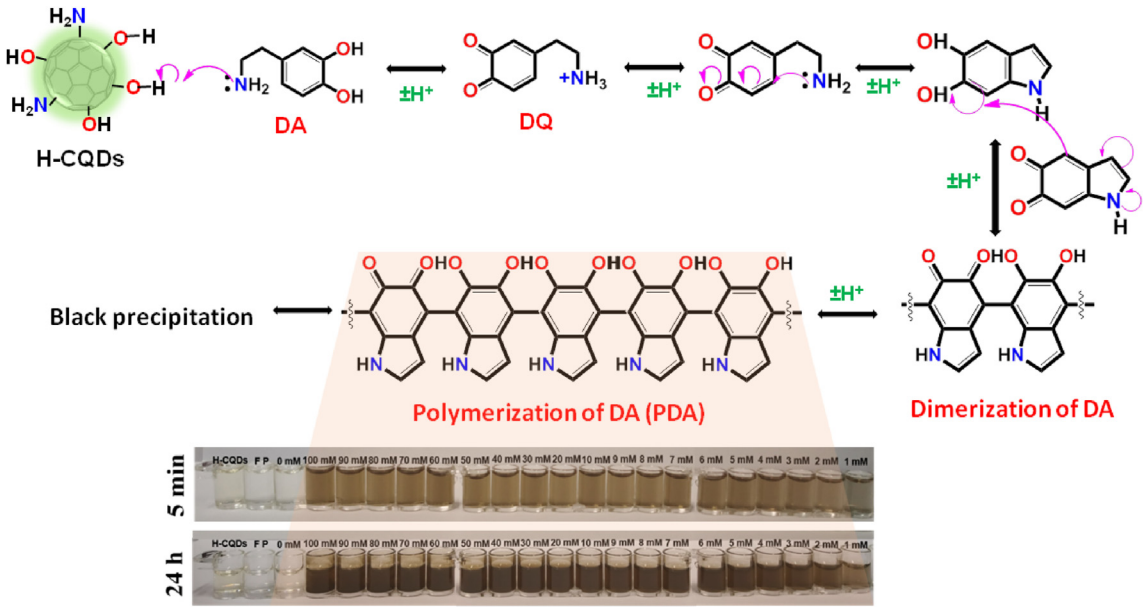

Fig. 5. Schematic illustration of plausible working mechanism for the formation of PDA from DA through polymerization process in real samples after 5 min and 24 h.

presented in Fig. S9.

3.2.2. Colorimetric sensor array-based reader system for DA detection

DA was colorimetrically detected, and the results were analyzed by visual inspection with the naked eye and were subsequently quantified using UV–vis spectroscopy. When DA (1000 μM–100 mM) was added to the H-CQDs, the pale yellow H-CQDs changed to light brown after 5 min (Fig. 7a), while the corresponding UV–vis spectrum exhibited a peak at approximately 305 nm, which was attributed to the formation of dopaquinone from DA oxidation (Fig. 7b) due to surface hydroxyl groups and oxygen [54,55]. After 24 h, the reaction mixture changed from light to dark brown (Fig. 7a), and the corresponding UV spectrum exhibited a peak at approximately 400 nm (Fig. 7c) which was attributed to the formation of polydopamine (PDA) by aggregation [56]. Thus, to characterize the DA induced color change, we used an absorbance ratio of 400 nm (A_{400}) to 305 nm (A_{305}) to obtain a regression coefficient of $R^2 = 0.987$, and the corresponding detection limit was 163 μM (Fig. S10). A representative image of the various DA concentrations is shown in Fig. S11, and the different systems used to detect DA are summarized in Table 1. All the other previously reported techniques were used additives like tetramethylbenzidine (TMB), H_2O_2, copper ions, PVP, etc., with nanoparticles to detect DA. In this system, without using any additives and functionalization of carbon quantum dots, sensed dopamine compared with reported techniques. However, based on the experimental results, the developed H-CQDs were also able to detect the DA in DI water and geriatric plasma and results were considerable for the point of care analytic view.

In addition to quantifying DA detection based on UV–vis spectroscopy, changes in sample color were effectively analyzed using a colorimetric sensor array-based system consisting of a 30 × 30 × 4 mm, 6 × 6

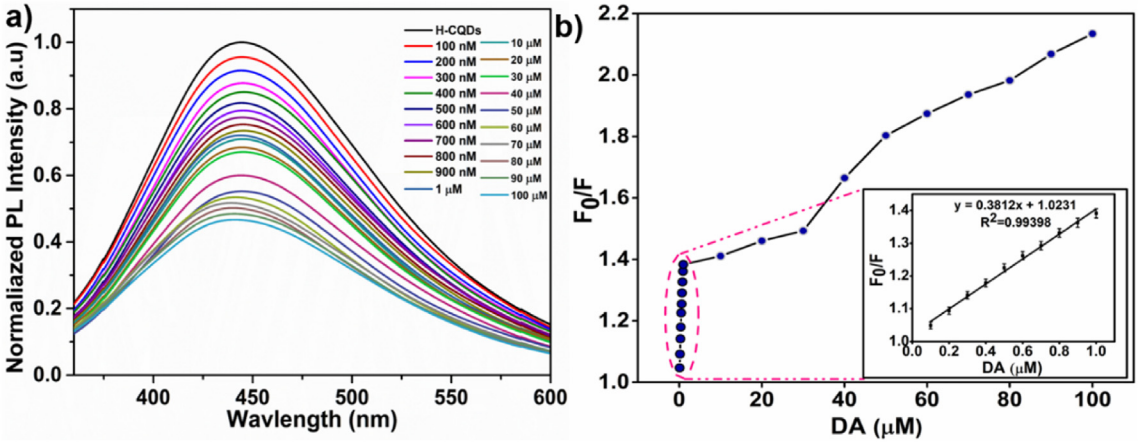

Fig. 6. a) Fluorescence spectrum of H-CQDs in the presence of different concentration of DA, (b) Linear relationship between F_0/F and the concentration of DA in the range of 100 nM-1 μM.

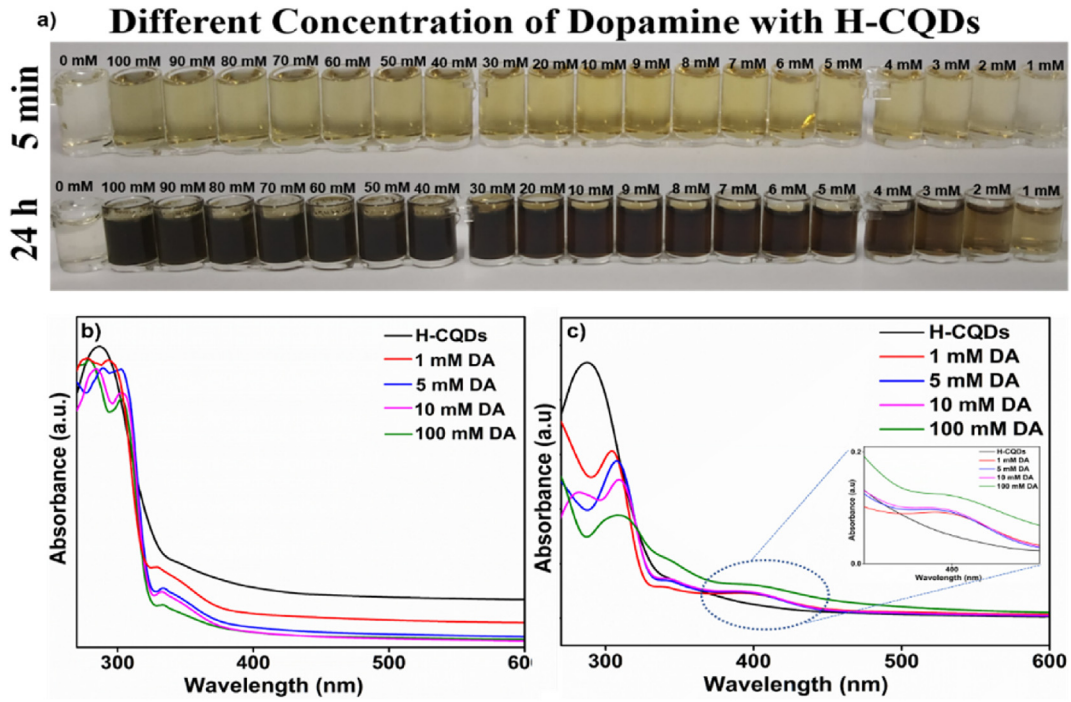

Fig. 7. a) Photographs of H-CQDs in presence of varies concentration of DA. UV–vis absorption spectrum of H-CQDs in presence of varies concentration of DA (b) 5 min and (c) 24 h. Inset: Zoomed in image of UV–visible spectrum of H-CQDs in presence of varies concentration of DA.

Table 1
A comparison of different detecting system for DA determination.

Probe + Additive used	Technique	Linear range	Limit of detection	Reference
Carbon dots + Chitosan	Electrochemical sensor	0.1–30 μM	11.2 nM	[60]
Adenosine capped QDs	Fluorescent sensor	0.1–20 μM	29.3 nM	[61]
Carbon quantum dots	Fluorescence quenching	0.2–100 mM	0.2 mM	[31]
Carbon dots	Fluorescence quenching	33–1250 μM	33 μM	[62]
Graphene quantum dots + dithienotetraphenylsilane	Fluorescent sensor	1–200 μM	80 nM	[63]
Gold nanoparticles + 3,3′,5,5′-tetramethylbenzidine (TMB) and H_2O_2	Colorimetric sensing	0.07–24 μM	0.025 μM	[64]
Silver nanoparticles + task-specific pyridinum ionic liquid	Colorimetric sensing	0.1–7.5 μM	0.031 μM	[65]
Silver nanoparticles + polyvinylpyrrolidone (PVP)	Colorimetric sensing	3.2 μM- 2.0 × 10^{-5} M	1.2 μM	[66]
H-CQDs - No additive added	Fluorometric and colorimetric sensor array reader system	100 nM-100 μM and 1000 μM-100 mM	8 nM and 163 μM	This work

array substrate fabricated with sensors consisting of ⌀4 mm wells that could hold approximately 50 μL samples. H-CQDs mixed with different concentrations of DA were added to the wells, and the white LED/UV light was illuminated from the bottom of the sensor matrix. The smartphone was placed on top of the system to image the sensor array with a color array analysis application. The detailed structure of the sensor array-based system is shown in Fig. S12.

Samples containing H-CQDs treated with different concentrations of DA were added to the wells on the sensor spots, and the array was imaged using the smartphone camera at 0, 5, and 60 min (1 h). The obtained images were analyzed using the analysis gel array application. The centers of the individual spots were calculated using the circle Hough transform algorithm. The analysis areas obtained using the algorithm overlapped the images obtained prior to and after DA detection, yielding red/green/blue (RGB) values and the associated differences and deviations in the RGB values of the images [57]. In turn, the program extracted the median, mean, and standard deviation of the RGB values obtained for the spots and sensor array images into an Excel file, and respective virtual array images were saved for the differences in the RGB values (Fig. 8a and b). The detailed procedure for sample imaging and data analysis is presented in Fig. S13.

3.2.3. *Detection of DA in geriatric plasma*

The pretreatment of the sample is carried out according to the steps of experimental part. After that, the standard addition method was used to test the content of DA in real samples with fluorometry and colorimetry. The PL intensity of the H-CQDs was gradually quenched up to 45% (Fig. 9a), the regression coefficient was $R^2 = 0.985$ (Fig. 9b), and the LOD

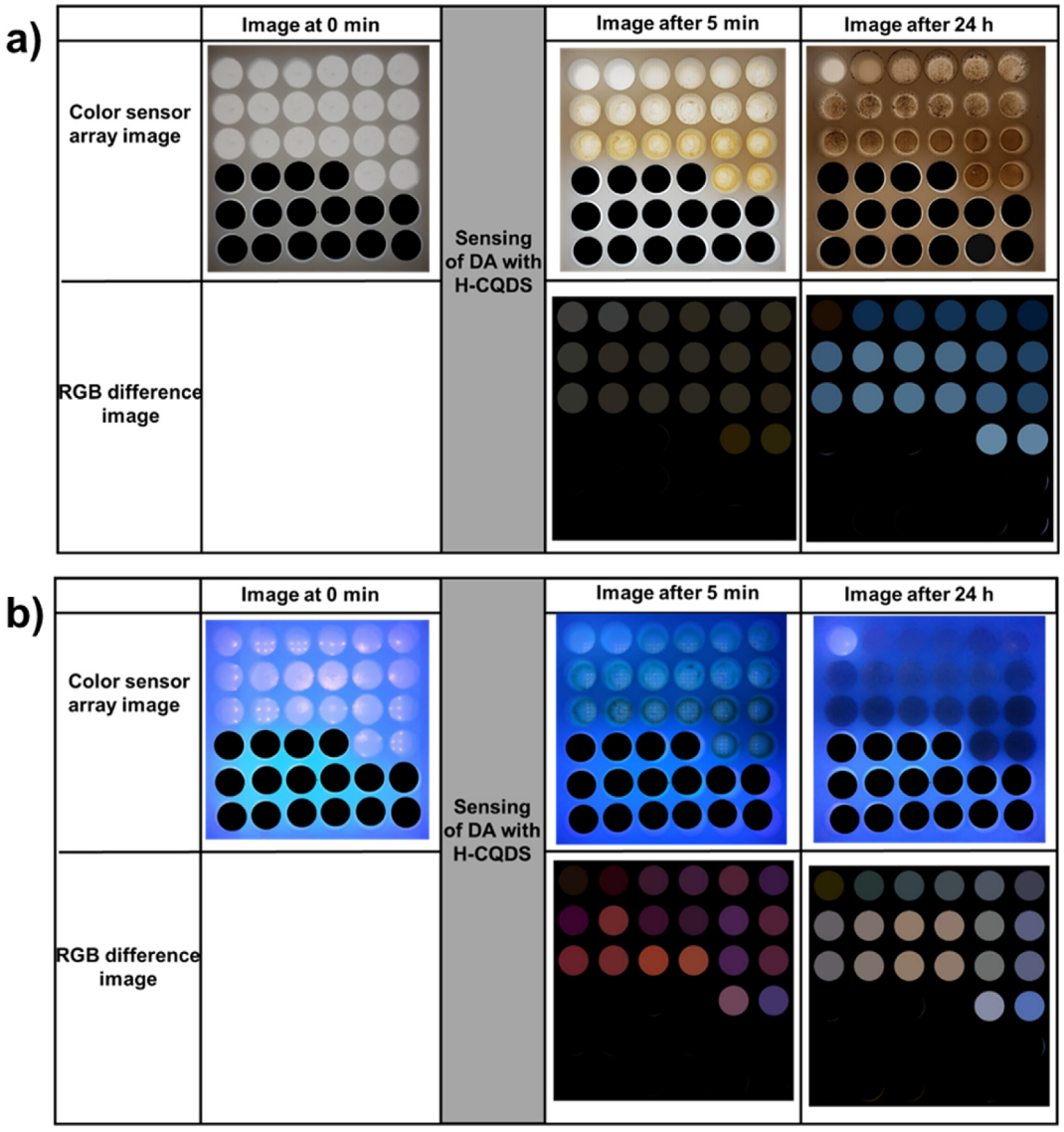

Fig. 8. a) The images of color sessor array and the analysis results of the RGB difference of the color sensor array of H-CQDs with different concentration of DA. The light source used is white LED. b) The images of color sessor array and the analysis results of the RGB difference of the color sensor array of H-CQDs with different concentration of DA. The light source used is UV light.

was calculated as 8.5 nM. The same procedure was repeated using female geriatric plasma for which the PL intensity of the H-CQDs was quenched 40% (Fig. 9c), the regression coefficient was $R^2 = 0.982$ (Fig. 9d), and the LOD was calculated as 8 nM. In addition, the emission spectra were slightly blue shifted. We hypothesized that the markedly increased concentration of amino acids in the plasma of elderly females may have increased the energy gap between the ground and excited states of the chromophore, thereby blue shifting the spectrum [58,59]. The recovery values ranged from 97 to 105%. These results indicated that H-CQDs could be employed as fluorescent probes to detect DA in biological samples. In case of colorimetric sensing, the color changes were observed with the naked eye. The pale yellow H-CQDs changed to light brown within 5 min and turned blackish brown after 24 h. Representative colorimetric images of the H-CQDs mixed with DA and male and female geriatric plasmas are shown in Fig. 9e. The absorption spectra generated for the mixtures after 5 min and 24 h are presented in Fig. S14a–d, respectively.

The DA concentration in the spiked male and female geriatric plasma was measured using HPLC as a reference method. The results obtained using our DA detection system and HPLC are compared in Table S2. Interestingly, the results obtained using HPLC were consistent with those obtained using the developed fluorescence and colorimetric approaches (Fig. S15).

3.2.4. *Specificity of dual-mode DA detection system*

Initially, we determined how Na^+, K^+, Glu, Cl^-, Mg^{2+}, Ca^{2+}, urea, creatinine, ammonia iron (Fe^{2+} and Fe^{3+}), zinc (Zn^{2+}), aluminum (Al^{3+}), UA, glutathione (GSH), L-aspartate (L-Asp), L-cysteine (L-Cys), Albumin interfered with DA detection in DI water. The PL spectra (Fig. S16) showed that only DA quenched the PL intensity of the H-CQDs and that the remaining interferents did not affect the PL intensity. With the same interferents, we fluorometrically detected DA in the male and female geriatric plasmas separately. The obtained PL spectra (Fig. S17a and b, respectively) again showed that other than DA, the remaining interferents did not quench the PL intensity of the H-CQDs in either the male or female geriatric plasma.

In colorimetric detection mode, Fig. S18 clearly shows that the color was only altered in the well containing both DA and H-CQDs. The colors in the wells containing the other interferents did not change. The same interference study was performed using the male and female geriatric

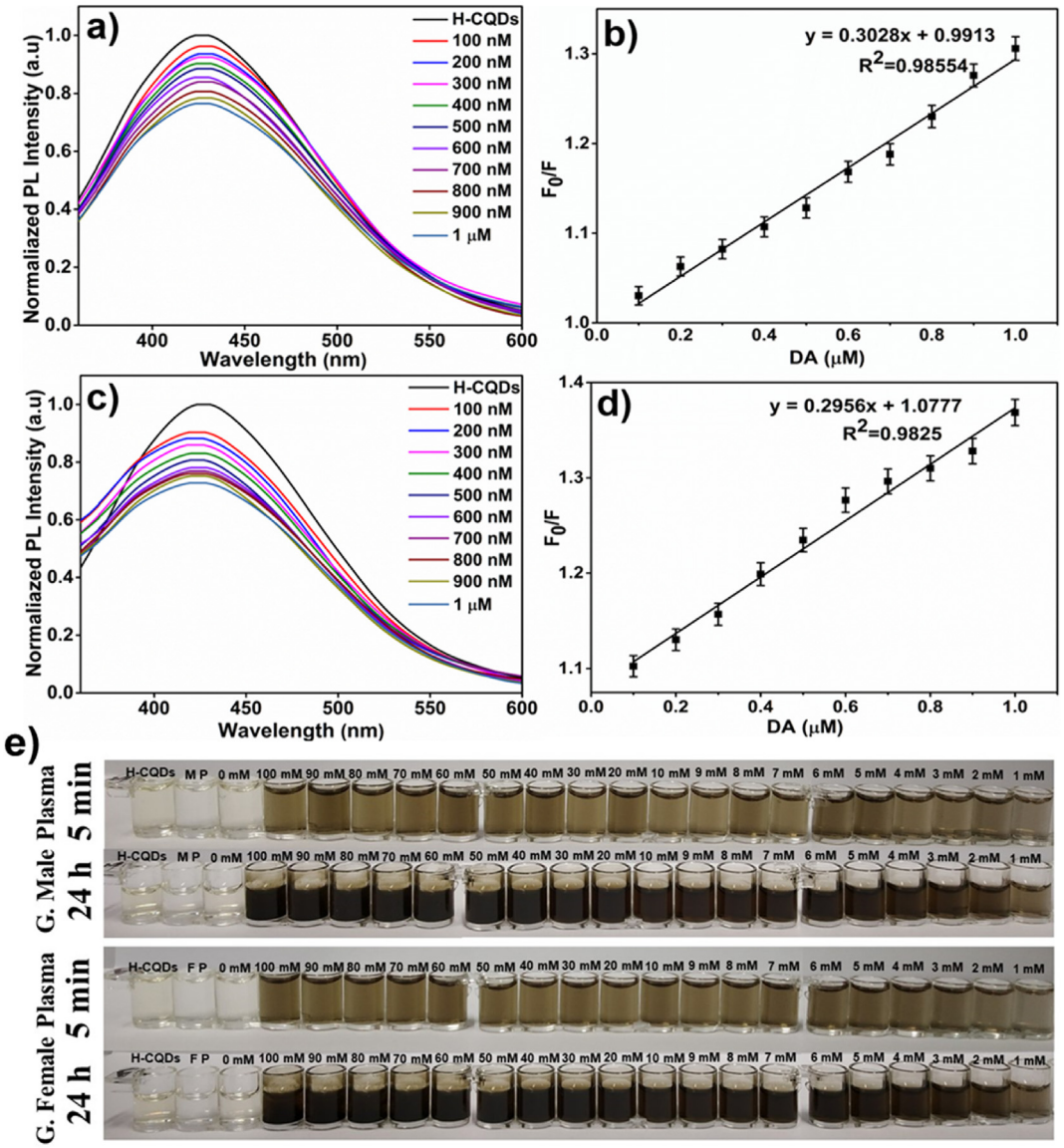

Fig. 9. (a) Fluorescence spectrum of H-CQDs in the presence of different concentration of DA in male geriatric plasma (b) Corresponding Linear regression plot of H-CQDs in male geriatric plasma, (c) Fluorescence spectrum of H-CQDs in the presence of different concentration of DA in female geriatric plasma, (d) Corresponding Linear regression plot of H-CQDs in female geriatric plasma, e) Photographs of H-CQDs in presence of varies concentration of DA in male and female geriatric plasma.

plasma separately, and similar results were obtained. Fig. S19 a and b show representative images of the interference study conducted using the male and female geriatric plasma, respectively. The results confirmed that our proposed system had selectively detected DA in both DI water and biological samples.

4. Conclusion

In conclusion, by exploiting the quick synthesis of 1–6 nm H-CQDs exhibiting bluish-green fluorescence and a QY of ~46%, we developed an electron transfer based dual-mode DA detection system (fluorometric sensor) and a colorimetric sensor array-based system to detect DA in aqueous media and male and female geriatric plasma. Because the DA detection system did not require any additives or functionalized H-CQDs, the system was cost effective. The enhanced properties of the H-CQDs enabled the proposed system to effectively detect DA over a wide linear range of concentrations up to the nanomolar level. The electron transfer and color change of the H-CQDs rendered the system effective and consistent for DA detection. Additionally, the proposed DA detection system was much easier to operate than conventional ones owing to simple PL measurements and the visual inspection of color changes through a smartphone-integrated sensor array-based system in a response time of approximately 5 min. Moreover, the proposed system provided effective, consistent, quantitative, and qualitative DA detection results on par with those achieved using HPLC. The results showed that our approach may be useful for developing a highly sensitive, selective, environmentally friendly, and cost effective DA detection system for application to the clinical diagnosis of geriatric patients.

Credit author statement

Gayathri Chellasamy: Conceptualization; Design of methodology; Formal analysis; Investigation; Data curation; Writing – original draft. **Seshadri Reddy Ankireddy:** Formal analysis; Data curation. **Kook-Nyung Lee:** Design of methodology; Data curation. **Saravanan Govindaraju:** Resources; Visualization; Supervision; Project administration. **Kyusik Yun:** Resources; Supervision; Writing-review & editing; Project administration; Funding acquisition.

Declaration of competing interest

The authors declare that they have no known competing financial interests or personal relationships that could have appeared to influence the work reported in this paper.

Acknowledgements

This research was supported by Basic Science Research Program through the National Research Foundation of Korea (NRF) funded by the Ministry of Education (2021R1A6A1A03038996).

Appendix A. Supplementary data

Supplementary data to this article can be found online at https://doi.org/10.1016/j.mtbio.2021.100168.

References

[1] S. Govindaraju, S.R. Ankireddy, B. Viswanath, J.S. Kim, K.S. Yun, Fluorescent gold nanoclusters for selective detection of dopamine in cerebrospinal fluid, Sci. Rep. 7 (2017) 40298.
[2] A. Vázquez-Guardado, S. Barkam, M. Peppler, A. Biswas, W. Dennis, S. Das, S. Seal, D. Chanda, Enzyme-free plasmonic biosensor for direct detection of neurotransmitter dopamine from whole blood, Nano Lett. 19 (2018) 449–454.
[3] K. Jackowska, P. Krysinski, New trends in the electrochemical sensing of dopamine, Anal. Bioanal. Chem. 405 (2013) 3753–3771.
[4] A.F.T. Arnsten, M. Wang, C.D. Paspalas, Dopamine's actions in primate prefrontal cortex: challenges for treating cognitive disorders, Pharmacol. Rev. 67 (2015) 681–696.
[5] S.K. Arumugasamy, S. Govindaraju, K. Yun, Electrochemical sensor for detecting dopamine using graphene quantum dots incorporated with multiwall carbon nanotubes, Appl. Surf. Sci. 508 (2020) 145294.
[6] X. Liu, J. Liu, Biosensors and sensors for dopamine detection, View 2 (2021) 20200102.
[7] M.A. Fotopoulou, P.C. Ioannou, Post-column terbium complexation and sensitized fluorescence detection for the determination of norepinephrine, epinephrine and dopamine using high-performance liquid chromatography, Anal. Chim. Acta 462 (2002) 179–185.
[8] Y. Zhao, S. Zhao, J. Huang, F. Ye, Quantum dot-enhanced chemiluminescence detection for simultaneous determination of dopamine and epinephrine by capillary electrophoresis, Talanta 85 (2011) 2650–2654.
[9] T. Yoshitake, J. Kehr, K. Todoroki, H. Nohta, M. Yamaguchi, Derivatization chemistries for determination of serotonin, norepinephrine and dopamine in brain microdialysis samples by liquid chromatography with fluorescence detection, Biomed. Chromatogr. 20 (2006) 267–281.
[10] J.E. Koehne, M. Marsh, A. Boakye, B. Douglas, I.Y. Kim, S.Y. Chang, D.P. Jang, K.E. Bennet, C. Kimble, R. Andrews, M. Meyyappan, Carbon nanofiber electrode array for electrochemical detection of dopamine using fast scan cyclic voltammetry, Analyst 136 (2011) 1802–1805.
[11] W. Shu, Y. Wang, C. Liu, R. Li, C. Pei, W. Lou, S. Lin, W. Di, J. Wan, Construction of a plasmonic chip for metabolic analysis in cervical cancer screening and evaluation, Small Methods 4 (2020) 1900469.
[12] J. Liu, C. Cai, Y. Wang, Y. Liu, L. Huang, T. Tian, Y. Yao, J. Wei, R. Chen, K. Zhang, B. Liu, K. Qian, A biomimetic plasmonic nanoreactor for reliable metabolite detection, Adv. Sci. 7 (2020) 1903730.
[13] Y. Li, P. Kang, S. Wang, Z. Liu, Y. Li, Z. Guo, Ag nanoparticles anchored onto porous CuO nanobelts for the ultrasensitive electrochemical detection of dopamine in human serum, Sens. Actuators B Chem. 327 (2021) 128878.
[14] K. Zhou, D. Shen, X. Li, Y. Chen, L. Hou, Y. Zhang, J. Sha, Molybdenum oxide-based metal-organic framework/polypyrrole nanocomposites for enhancing electrochemical detection of dopamine, Talanta 209 (2020) 120507.
[15] S.K. Arumugasamy, G. Chellasamy, S. Gopi, S. Govindaraju, K.S. Yun, Current advances in the detection of neurotransmitters by nanomaterials: an update, Trends Anal. Chem. 123 (2019) 115766.
[16] Y. Tao, Y. Lin, J. Ren, X. Qu, A dual fluorometric and colorimetric sensor for dopamine based on BSA-stabilized Aunanoclusters, Biosens. Bioelectron. 42 (2013) 41–46.
[17] E.J.M. Moonen, J.R. Haakma, E. Peri, E. Pelssers, M. Mischi, J.M.J. den Toonder, Wearable sweat sensing for prolonged, semicontinuous, and nonobtrusive health monitoring, View 1 (2020) 20200077.
[18] M.J. Kangas, R.M. Burks, J. Atwater, R.M. Lukowicz, P. Williams, A.E. Holmes, Colorimetric sensor arrays for the detection and identification of chemical weapons and explosives, Crit. Rev. Anal. Chem. 47 (2017) 138–153.
[19] J. Lv, S. Feng, Y. Ding, C. Chen, Y. Zhang, W. Lei, Q. Hao, S. Chen, A high-performance fluorescent probe for dopamine detection based on g-C3N4 nanofibers, Spectrochim, Acta A Mol. Biomol. Spectrosc. 212 (2019) 300–307.
[20] C. Wang, H. Shi, M. Yang, Z. Yao, B. Zhang, E. Liu, X. Hu, W. Xue, J. Fan, Biocompatible sulfur nitrogen co-doped carbon quantum dots for highly sensitive and selective detection of dopamine, Colloids Surf., B 205 (2021) 111874.
[21] J. Zhao, L. Zhao, C. Lan, S. Zhao, Graphene quantum dots as effective probes for label-free fluorescence detection of dopamine, Sens. Actuators B Chem. 223 (2016) 246–251.
[22] N. Wang, M. Xie, M. Wang, Z. Li, X. Su, UiO-66-NH2 MOF-based ratiometric fluorescent probe for the detection of dopamine and reduced glutathione, Talanta 220 (2020) 121352.
[23] X. Tang, Y. Liu, X. Bai, H. Yuan, Y. Hu, X. Yu, X. Liao, Turn-on fluorescent probe for dopamine detection in solutions and live cells based on in situ formation of aminosilane-functionalized carbon dots, Anal. Chim. Acta 1157 (2021) 338394.
[24] N. Yusoff, A. Pandikumar, R. Ramaraj, H.N. Lim, N.M. Huang, Gold nanoparticle based optical and electrochemical sensing of dopamine, Microchim. Acta. 182 (2015) 2091–2114.
[25] A. Roda, E. Michelini, M. Zangheri, M.D. Fusco, D. Calabria, P. Simoni, Smartphone-based biosensors: a critical review and perspectives, Trends Anal. Chem. 79 (2016) 317–325.
[26] B. Kong, A. Zhu, Y. Luo, Y. Tian, Y. Yu, G. Shi, Sensitive and selective colorimetric visualization of cerebral dopamine based on double molecular recognition, Angew. Chem. 50 (2011) 1837–1840.
[27] Z. Chen, C. Zhang, T. Zhou, H. Ma, Gold nanoparticle based colorimetric probe for dopamine detection based on the interaction between dopamine and melamine, Microchim. Acta. 182 (2015) 1003–1008.
[28] J. Shen, C. Sun, X. Wu, Silver nanoprisms-based Tb (III) fluorescence sensor for highly selective detection of dopamine, Talanta 165 (2017) 369–376.
[29] H.B. Wang, H.D. Zhang, Y. Chen, K.J. Huang, Y.M. Liu, A label-free and ultrasensitive fluorescent sensor for dopamine detection based on double-stranded DNA templated copper nanoparticles, Sens. Actuators B Chem. 220 (2015) 146–153.
[30] P. Cui, Y. Kuai, Q. Wu, Y. Zheng, X. Liu, Synthesis of a fluorescent cation surfactant derived from carbon quantum dots, Mater. Lett. 235 (2019) 161–163.
[31] D. Bharathi, B. Siddlingeshwar, R.H. Krishna, V. Singh, N. Kottam, D.D. Divakar, A.A. Alkheraif, Green and cost effective synthesis of fluorescent carbon quantum dots for dopamine detection, J. Fluoresc. 28 (2018) 573–579.
[32] Y. Zhang, S. Qi, Z. Liu, Y. Shi, W. Yue, C. Yi, Rapid determination of dopamine in human plasma using a gold nanoparticle-based dual-mode sensing system, Mater. Sci. Eng. C 61 (2016) 207–213.
[33] K. Hashizume, A. Yamatodani, T. Ogihara, Free and total dopamine in human plasma: effects of posture, age and some pathophysiological conditions, Hypertens. Res. 18 (1995) S205–S207.
[34] J. Zhang, H. Wang, Y. Xiao, J. Tang, C. Liang, F. Li, H. Dong, W. Xu, A simple approach for synthesizing of fluorescent carbon quantum dots from tofu wastewater, Nanoscale Res. Lett. 12 (2017) 1–7.
[35] B. De, N. Karak, A green and facile approach for the synthesis of water soluble fluorescent carbon dots from banana juice, RSC Adv. 3 (2013) 8286–8290.
[36] B. Luo, H. Yang, B. Zhou, S.M. Ahmed, Y. Zhang, H. Liu, X. Liu, Y. He, S. Xia, Facile synthesis of Luffa sponge activated carbon fiber based carbon quantum dots with green fluorescence and their application in Cr (VI) determination, ACS Omega 5 (2020) 5540–5547.
[37] S. Lai, Y. Jin, L. Shi, R. Zhou, Y. Zhou, D. An, Mechanisms behind excitation-and concentration-dependent multicolor photoluminescence in graphene quantum dots, Nanoscale 12 (2020) 591–601.
[38] Z. Gan, H. Xu, Y. Hao, Mechanism for excitation-dependent photoluminescence from graphene quantum dots and other graphene oxide derivates: consensus, debates and challenges, Nanoscale 8 (2016) 7794–7807.
[39] S.R. Ankireddy, V.G. Vo, S.S.A. An, J.S. Kim, Solvent-free synthesis of fluorescent carbon dots: an eco-friendly approach for the bio-imaging and screening of anticancer activity via caspase-induced apoptosis, ACS Appl. Bio Mater. 3 (2020) 4873–4882.
[40] M. Moniruzzaman, J. Kim, N-doped carbon dots with tunable emission for multifaceted application: solvatochromism, moisture sensing, pH sensing, and solid state multicolor lighting, Sens. Actuators B Chem. 295 (2019) 12–21.
[41] J. Wang, S. Cao, Y. Ding, F. Ma, W. Lu, M. Sun, Theoretical investigations of optical origins of fluorescent graphene quantum dots, Sci. Rep. 6 (2016) 1–5.
[42] G. Kalaiyarasan, J. Joseph, Determination of vitamin B12 via pH-dependent quenching of the fluorescence of nitrogen doped carbon quantum dots, Microchim. Acta. 184 (2017) 3883–3891.
[43] S. Chaudhary, S. Kumar, B. Kaur, S.K. Mehta, Potential prospects for carbon dots as a fluorescence sensing probe for metal ions, RSC Adv. 6 (2016) 90526–90536.
[44] H. Muktha, R. Sharath, N. Kottam, S.P. Smrithi, K. Samrat, P. Ankitha, Green synthesis of carbon dots and evaluation of its pharmacological activities, BioNanoScience 10 (2020) 731–744.
[45] T. López, J.L. Bata-Garcia, D. Esquivel, E. Ortiz-Islas, R. Gonzalez, J. Ascencio, P. Quintana, G. Oskam, F.J. Álvarez-Cerevera, F.J. Heredia-López, J.L. Gongora-Alfaro, Treatment of Parkinson's disease: nanostructured sol–gel silica–dopamine reservoirs for controlled drug release in the central nervous system, Int. J. Nanomed. 6 (2011) 19–31.
[46] X. Yang, Y. Zhuo, S. Zhu, Y. Luo, Y. Feng, Y. Dou, Novel and green synthesis of high-fluorescent carbon dots originated from honey for sensing and imaging, Biosens. Bioelectron. 60 (2014) 292–298.
[47] L. Wu, X. Cai, K. Nelson, W. Xing, J. Xia, R. Zhang, A.J. Stacy, M. Luderer, G.M. Lanza, L.V. Wang, B. Shen, D. Pan, A green synthesis of carbon nanoparticles from honey and their use in real-time photoacoustic imaging, Nano Res. 6 (2013) 312–325.
[48] R.R. Gaddam, D. Vasudevan, R. Narayan, K.V.S.N. Raju, Controllable synthesis of biosourced blue-green fluorescent carbon dots from camphor for the detection of heavy metal ions in water, RSC Adv. 4 (2014) 57137–57143.

[49] P. Puech, M. Kandara, G. Paredes, L. Moulin, E. Weiss-Hortala, A. Kundu, N. Ratel-Ramond, J. Plewa, R. Pellenq, M. Monthioux, Analyzing the Raman spectra of graphenic carbon materials from kerogens to nanotubes: what type of information can be extracted from defect bands? C 5 (2019) 69.
[50] J.D. Ciubuc, K.E. Bennet, C. Qiu, M. Alonzo, W.G. Durrer, F.S. Manciu, Raman computational and experimental studies of dopamine detection, Biosensors 7 (2017) 43.
[51] M.H. Cheng, E. Block, F. Hu, M.C. Cobanoglu, A. Sorkin, I. Bahar, Insights into the modulation of dopamine transporter function by amphetamine, orphenadrine, and cocaine binding, Front. Neurol. 6 (2015) 134.
[52] J. Armstrong, R.B. Barlow, The ionization of phenolic amines, including apomorphine, dopamine and catecholamines and an assessment of zwitterion constants, Br. J. Pharmacol. 57 (1976) 501–516.
[53] I.L. Medintz, M.H. Stewart, S.A. Trammell, K. Susumu, J.B. Delehanty, B.C. Mei, J.S. Melinger, J.B. Blanco-Canosa, P.E. Dawson, H. Mattoussi, Quantum-dot/dopamine bioconjugates function as redox coupled assemblies for in vitro and intracellular pH sensing, Nat. Mater. 9 (2010) 676–684.
[54] J.H. Lin, C.J. Yu, Y.C. Yang, W.L. Tseng, Formation of fluorescent polydopamine dots from hydroxyl radical-induced degradation of polydopamine nanoparticles, Phys. Chem. Chem. Phys. 17 (2015) 15124–15130.
[55] Y. Li, N. Cai, M. Wang, W. Na, F. Shi, X. Su, Fluorometric detection of tyrosine and cysteine using graphene quantum dots, RSC Adv. 6 (2016) 33197–33204.
[56] W. Sheng, B. Li, X. Wang, B. Dai, B. Yu, X. Jia, F. Zhou, Brushing up from "anywhere" under sunlight: a universal surface-initiated polymerization from polydopamine-coated surfaces, Chem. Sci. 6 (2015) 2068–2073.
[57] S. Yoon, K.N. Lee, D. Hong, H.L. Kang, S. Song, W.H. Kim, W.K. Seong, D.S. Shin, H. Cho, H. Kim, Colorimetric sensor array reader system using smartphone camera, in: ECS Meeting Abstracts, vol. 34, IOP Publishing, 2020, p. 2399.
[58] B. Caballero, R.E. Gleason, R.J. Wurtman, Plasma amino acid concentrations in healthy elderly men and women, Am. J. Clin. Nutr. 53 (1991) 1249–1252.
[59] L. Canty, S. Hariharan, Q. Liu, S.A. Haney, D.W. Andrews, Peak emission wavelength and fluorescence lifetime are coupled in far-red, GFP-like fluorescent proteins, PLoS One 13 (2018), e0208075.
[60] Q. Huang, S. Hu, H. Zhang, J. Chen, Y. He, F. Li, W. Weng, J. Ni, X. Bao, Y. Lin, Carbon dots and chitosan composite film based biosensor for the sensitive and selective determination of dopamine, Analyst 138 (2013) 5417–5423.
[61] Q. Mu, H. Xu, Y. Li, S. Ma, X. Zhong, Adenosine capped QDs based fluorescent sensor for detection of dopamine with high selectivity and sensitivity, Analyst 139 (2014) 93–98.
[62] U. Baruah, N. Gogoi, A. Konwar, A, M.J. Deka, D. Chowdhury, G. Majumdar, Carbon dot based sensing of dopamine and ascorbic acid, J. Nanoparticles (2014) 178518, 2014.
[63] S. Baluta, K. Malecha, D. Zając, J. Sołoducho, J. Cabaj, Dopamine sensing with fluorescence strategy based on low temperature co-fired ceramic technology modified with conducting polymers, Sens. Actuators B Chem. 252 (2017) 803–812.
[64] C. Jiang, S. Pang, J. Luo, X. Liu, W. Guo, W. Jiang, Colorimetric sensing of dopamine based on peroxidase-like activity of gold nanoparticles, J. Anal. Chem. 74 (2019) 679–685.
[65] S. Rostami, A. Mehdinia, A. Jabbari, E. Kowsari, R. Niroumand, T.J. Booth, Colorimetric sensing of dopamine using hexagonal silver nanoparticles decorated by task-specific pyridinum based ionic liquid, Sens. Actuators B Chem. 271 (2018) 64–72.
[66] M.H. Nezhad, J. Tashkhourian, J. Khodaveisi, Sensitive spectrophotometric detection of dopamine, levodopa and adrenaline using surface plasmon resonance band of silver nanoparticles, J. Iran. Chem. Soc. 7 (2010) S83–S91.